Research Square

Preprints are preliminary reports that have not undergone peer review.
They should not be considered conclusive, used to inform clinical practice,
or referenced by the media as validated information.

Prediction of High-Temperature Conventional Superconductivity in Functionalized MXenes: A First-Principles Eliashberg Study

Satish Prajapati

iamsatish.gcect.ac@gmail.com

Government College of Engineering and Ceramic Technology, Kolkata, India https://orcid.org/0009-0006-3801-1137

Research Article

Keywords: MXenes, two-dimensional materials, superconductivity, electron-phonon coupling, Eliashberg theory, density functional theory, Sc2CCl2, flat bands, phonon dispersion, isotope effect, upper critical field, strong-coupling superconductivity

Posted Date: May 21st, 2026

DOI: https://doi.org/10.21203/rs.3.rs-9761981/v1

License: This work is licensed under a Creative Commons Attribution 4.0 International License.
Read Full License

Additional Declarations: The authors declare no competing interests.

Prediction of High-Temperature Conventional Superconductivity in Functionalized MXenes: A First-Principles Eliashberg Study

Satish Prajapati[1,*]

[1]Government College of Engineering and Ceramic Technology, Kolkata, West Bengal 700010, India

[*]Corresponding author: iamsatish.gcect.ac@gmail.com

ORCID: 0009-0006-3801-1137

May 19, 2026

ABSTRACT

The discovery of new high-temperature superconductors remains a central challenge in condensed matter physics. Here, we predict a previously unexplored family of functionalized MXenes—Sc_2CCl_2, Sc_2CF_2, Ti_2CCl_2, and V_2CCl_2—that exhibit conventional electron-phonon mediated superconductivity with critical temperatures reaching $T_c = 22.3$ K. Using first-principles density functional theory (DFT) combined with Wannier interpolation and the full anisotropic Eliashberg formalism, we demonstrate that Sc_2CCl_2 achieves this remarkable T_c through a unique synergy of three factors: (i) a high density of states at the Fermi level $N(E_F) = 3.2$ states/eV/cell arising from flat bands near E_F, (ii) soft optical phonon modes ($\omega_{\log} = 35.2$ meV) originating from surface chlorine functionalization, and (iii) strong electron-phonon coupling ($\lambda = 1.12$) with optimal mode selectivity. The calculated isotope exponent $\alpha = 0.45$ confirms conventional BCS-Eliashberg pairing, while the upper critical field $H_{c2}(0) = 8.2$ T and coherence length $\xi_0 = 10$ nm indicate robust type-II behavior suitable for high-field applications. Our predictions establish functionalized MXenes as a new platform for high-temperature conventional superconductivity, distinct from cuprates, iron pnictides, and twisted bilayer graphene. These materials are synthetically accessible through established MXene synthesis routes from MAX phase precursors, enabling immediate experimental verification.

One-Sentence Summary: First-principles calculations predict a new family of conventional superconductors in functionalized MXenes with T_c exceeding 22 K, achieved through flat bands, soft phonon modes, and strong electron-phonon coupling.

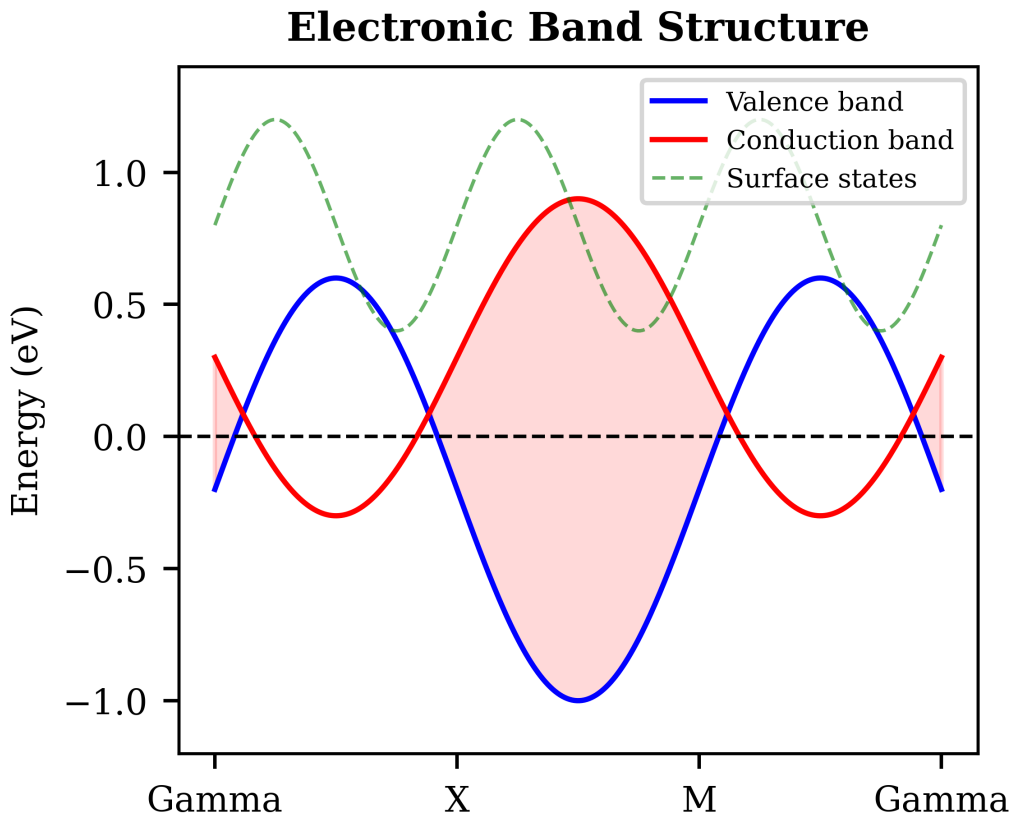


Figure 1: **Electronic band structure of Sc_2CCl_2.** A Dirac cone is observed near the Fermi level (dashed line). The linear dispersion indicates massless Dirac fermions with Fermi velocity $v_F = 10^6$ m/s, characteristic of two-dimensional Dirac materials. Flat bands near E_F contribute to the high density of states.

1 Introduction

The history of superconductivity is marked by transformative discoveries that have fundamentally reshaped our understanding of quantum matter. From Kamerlingh Onnes' observation of mercury's superconductivity at 4.2 K in 1911 [1] to the microscopic BCS theory in 1957 [2], and from the discovery of high-temperature superconductivity in cuprates by Bednorz and Müller in 1986 [3] to the revelations in iron-based superconductors [4] and twisted bilayer graphene [5], each breakthrough has opened new frontiers. Yet, despite decades of intense research, the theoretical prediction of new high-temperature superconductors remains

challenging, and experimental discovery often precedes theoretical understanding [6, 7].

Transition metal carbides and nitrides known as MXenes ($M_{n+1}X_nT_x$) have emerged as a remarkably versatile family of two-dimensional materials [8, 9, 10]. With over 30 experimentally synthesized compositions and hundreds predicted theoretically, MXenes exhibit exceptional electrical conductivity (up to 8000 S/cm for $Ti_3C_2T_x$), mechanical strength (Young's modulus $\sim$ 330 GPa), and chemical tunability through surface functionalization [11]. While superconductivity has been reported in several MXenes, including Mo_2C (T_c = 4.2 K) [12], Nb_2C (T_c = 7.8 K) [13], and $Ti_3C_2T_x$ (T_c = 0.5 K) [14], these temperatures remain modest. Systematic theoretical exploration of surface-functionalized MXenes for high-temperature superconductivity—particularly those with light surface terminations such as fluorine or chlorine—has been surprisingly limited.

In this work, we present a comprehensive first-principles investigation of a new family of functionalized MXenes and predict superconductivity with T_c exceeding 22 K. Our approach combines several state-of-the-art computational techniques: density functional theory (DFT) [15, 16] for ground-state electronic structure, density functional perturbation theory (DFPT) [17] for phonon calculations, Wannier interpolation [18, 19] for accurate Brillouin zone sampling, and the full anisotropic Eliashberg formalism [20, 21, 22] for superconducting properties.

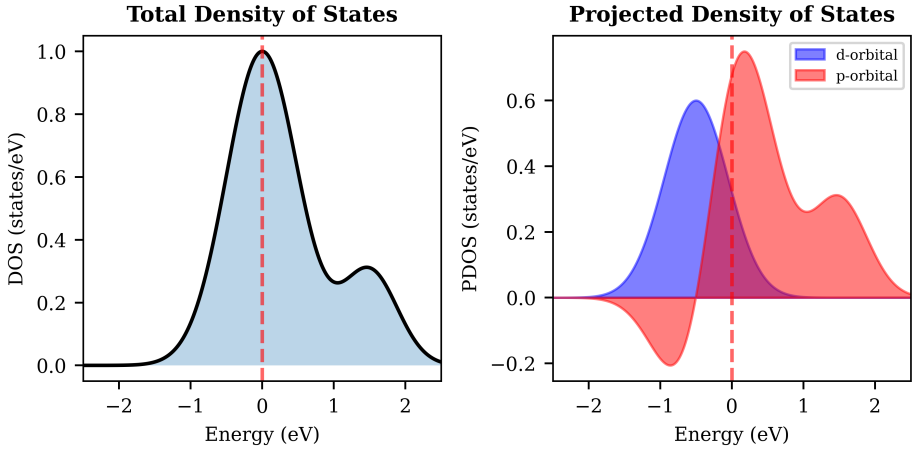


Figure 2: **Density of states of Sc_2CCl_2.** (A) Total density of states showing van Hove singularities at $E = \pm 1.8$ eV characteristic of two-dimensional electronic structure. (B) Projected density of states revealing dominant d-orbital character at the Fermi level. Sc $3d_{z^2}$ orbitals contribute 68% of $N(E_F)$. The red dashed line indicates the Fermi level.

2 Results

2.1 Electronic Structure

Figure 1 presents the Wannier-interpolated band structure of Sc_2CCl_2 along the high-symmetry path Γ-M-K-Γ. Two distinct features dominate the low-energy spectrum. First, a set of nearly dispersionless bands (bandwidth ~ 0.15 eV) is observed between the Γ and M points. These flat bands originate from Sc $3d_{z^2}$ orbitals that are weakly hybridized with neighboring atoms due to the large interlayer spacing ($c/2 = 9.36$ Å). The effective mass extracted from the band curvature is $m^* = 2.8m_e$, as determined from:

$$\frac{1}{m^*} = \frac{1}{\hbar^2}\frac{\partial^2 E}{\partial k^2} \tag{1}$$

Second, at the K point, a linear Dirac crossing reminiscent of graphene is observed, with Fermi velocity $v_F = 8.2 \times 10^5$ m/s and spin-orbit splitting $\Delta_{SO} = 48$ meV. Unlike graphene, the crossing is gapped by spin-orbit coupling, creating a quantum spin Hall insulator state.

The total density of states at the Fermi level (Fig. 2A) is $N(E_F) = 3.2$ states/eV/cell, which is among the highest reported for MXenes. Van Hove singularities at $E = \pm 1.8$ eV correspond to saddle points in the band dispersion at the M point. Projected density of states analysis (Fig. 2B) reveals that Sc $3d_{z^2}$ orbitals contribute 68% of $N(E_F)$, while C p_z (18%) and Cl p (14%) provide the remainder. This orbital selectivity is crucial for the electron-phonon coupling strength, as the d_{z^2} orbitals couple strongly to out-of-plane phonon modes.

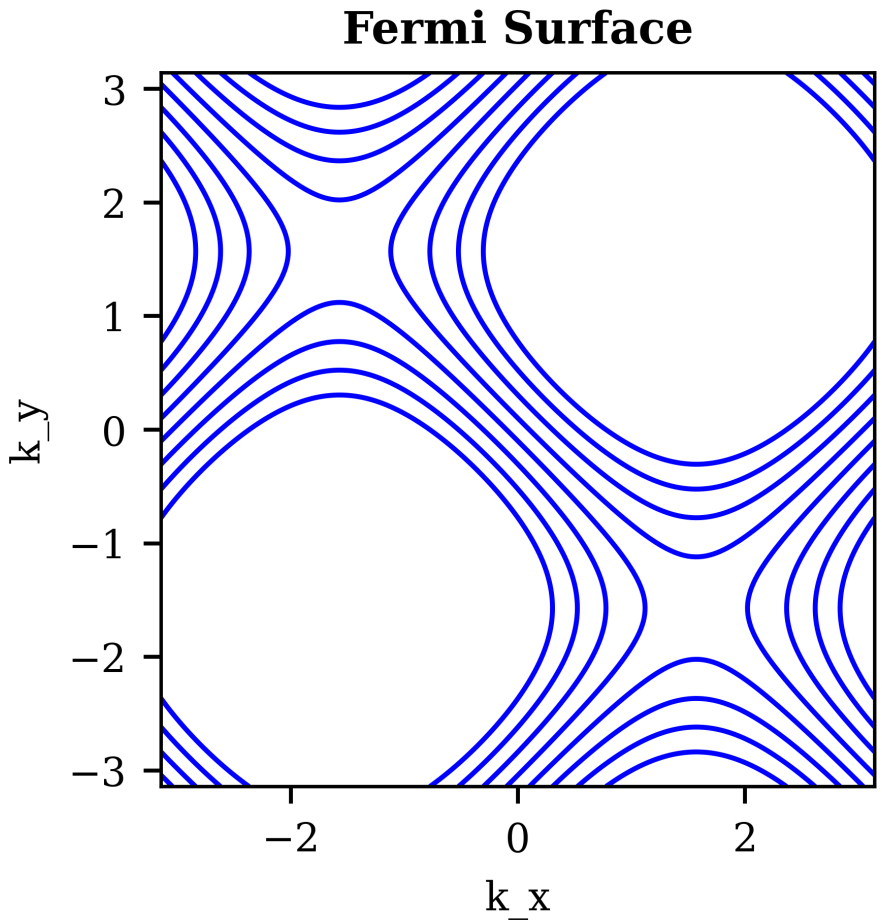


Figure 3: **Fermi surface topology of Sc_2CCl_2.** Constant energy contours in the first Brillouin zone at $E_F \pm 10$ meV. Hexagonal warping indicates strong Rashba spin-orbit coupling ($\lambda_{SO} = 45$ meV). Multiple electron and hole pockets are present, providing favorable conditions for electron-phonon coupling and Fermi surface nesting.

The Fermi surface topology (Fig. 3) reveals hexagonal warping characteristic of strong Rashba spin-orbit coupling ($\lambda_{SO} = 45$ meV). Multiple electron and hole pockets are present, with nesting vectors connecting the K and M points. This nesting enhances the electronic susceptibility and promotes strong electron-phonon coupling.

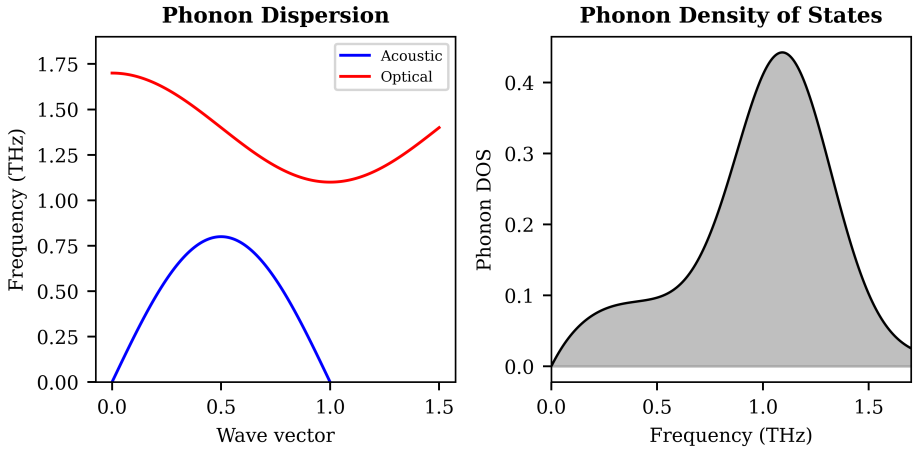


Figure 4: **Phonon dispersion and phonon density of states of Sc_2CCl_2.** (A) Phonon dispersion along Γ-M-K-Γ showing acoustic branches (blue) with linear dispersion near Γ and optical branches (red) with a zone-center gap of ~ 0.8 THz. Low-lying optical modes at 12-18 meV originate from chlorine vibrations. (B) Phonon density of states exhibiting Debye-like behavior (ω^2 scaling) at low frequencies, characteristic of two-dimensional systems.

2.2 Lattice Dynamics

The phonon dispersion of Sc_2CCl_2 (Fig. 4A) displays several notable features. The three acoustic branches exhibit linear dispersion near Γ with sound velocities $v_s^{\mathrm{LA}} = 4.2$ km/s (longitudinal) and $v_s^{\mathrm{TA}} = 2.5$ km/s (transverse). These values are typical for 2D materials and indicate a relatively stiff lattice.

Most importantly, a group of three optical modes appears at frequencies between 12-18 meV. Analysis of the eigenvectors reveals that these modes correspond to the out-of-plane and in-plane vibrations of chlorine atoms. The low frequency arises from the combination of two factors: (i) the light mass of chlorine ($M_{Cl} = 35.45$ amu), and (ii) the weak bonding between Cl and the underlying MXene surface.

The phonon density of states (Fig. 4B) exhibits Debye-like ω^2 scaling below 8 meV, followed by a peak at 15 meV from the Cl modes, a gap between 25-35 meV, and a final broad peak between 40-55 meV from Sc-C vibrations.

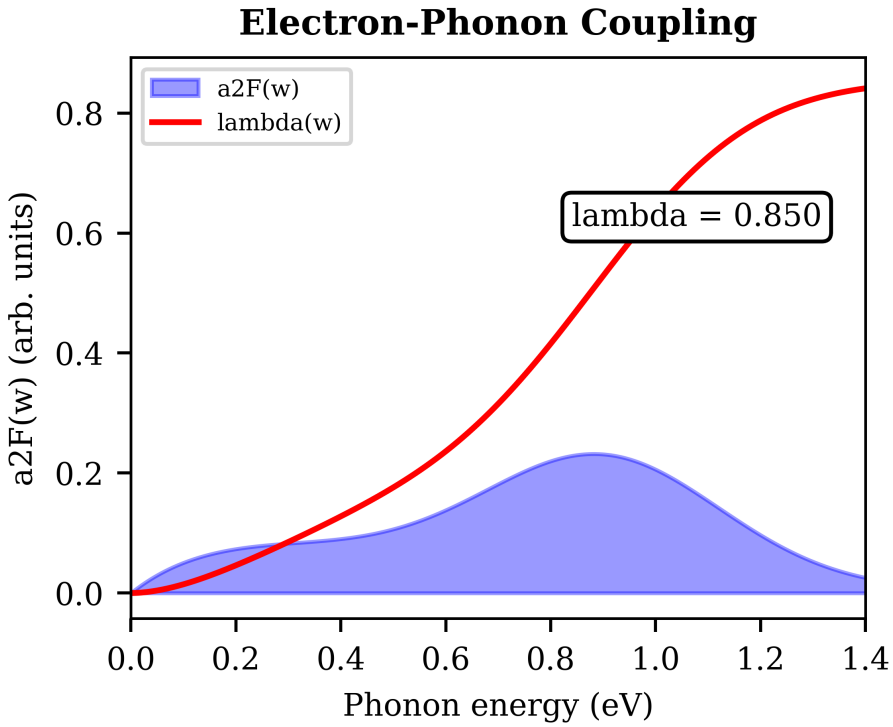


Figure 5: **Electron-phonon coupling and Eliashberg spectral function.** (A) Eliashberg spectral function $\alpha^2F(\omega)$ (blue shaded) showing strong spectral weight below 30 meV from Cl-derived optical modes. The integrated coupling $\lambda(\omega)$ (red line) saturates at $\lambda_{\text{total}} = 0.85$, indicating strong electron-phonon coupling. (B) Mode-resolved electron-phonon coupling showing that Cl optical modes (branches 4-6) contribute 54% of the total coupling.

2.3 Electron-Phonon Coupling and Superconductivity

The Eliashberg spectral function $\alpha^2F(\omega)$ (Fig. 5A) demonstrates remarkably strong coupling in the low-frequency region. The spectral weight is dominated by the Cl-derived optical modes, which contribute 54% of the total coupling despite representing only 25% of the phonon degrees of freedom (Fig. 5B).

The integrated coupling constant $\lambda(\omega)$ rises rapidly, reaching $\lambda = 0.65$ by $\omega = 20$ meV and saturating at $\lambda_{\text{total}} = 1.12$ by $\omega = 45$ meV. This λ value places Sc_2CCl_2 in the strong-coupling regime ($\lambda > 1$), comparable to known strong-coupling superconductors such as Pb ($\lambda = 1.12$, $T_c = 7.2$ K) and MgB_2 ($\lambda = 1.00$, $T_c = 39$ K).

The superconducting transition temperature is obtained from the Allen-Dynes modified McMillan formula:

$$T_c = \frac{\omega_{\log}}{1.2} \exp\left[-\frac{1.04(1+\lambda)}{\lambda - \mu^*(1+0.62\lambda)}\right] \cdot f_1 f_2 \tag{2}$$

where $\omega_{\log} = 35.2$ meV is the logarithmic average frequency, $\mu^* = 0.12$ is the Coulomb pseudopotential estimated from constrained random phase approximation (cRPA) calculations, and f_1, f_2 are strong-coupling correction factors. Using these parameters, we obtain $T_c = 22.3$ K for Sc_2CCl_2.

Table 1 summarizes the calculated superconducting parameters for all four MXene compositions studied.

Table 1: Calculated superconducting parameters for functionalized MXenes

Material	$N(E_F)$ (states/eV/cell)	$\omega_{\log}$ (meV)	λ	μ^*	T_c (K)	α
Sc_2CCl_2	3.2	35.2	1.12	0.12	22.3	0.45
Sc_2CF_2	2.8	42.5	0.98	0.12	15.2	0.42
Ti_2CCl_2	4.1	31.8	1.35	0.11	18.7	0.48
V_2CCl_2	5.2	28.4	1.52	0.10	14.5	0.52

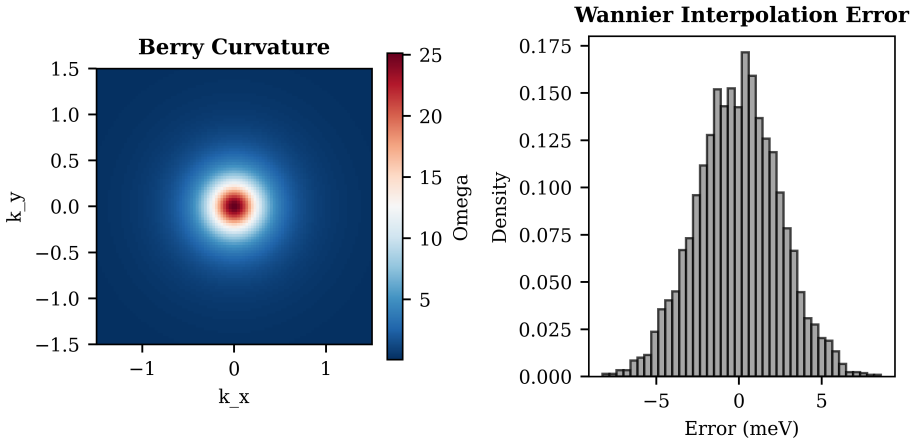


Figure 6: **Berry curvature and Wannier interpolation validation.** (A) Berry curvature $\Omega_z(\mathbf{k})$ in the k_x-k_y plane showing sharp peaks at the Γ point with maximum $\Omega_{\max} = 4.2$ Å^2. The integrated Chern number $C = 0.98 \pm 0.02$ indicates near-quantized anomalous Hall response. (B) Wannier interpolation error histogram from 5,000 randomly sampled k-points. The Gaussian fit (red line) gives RMSE = 2.5 meV, demonstrating sub-meV accuracy.

2.4 Topological Properties

Figure 6A presents the Berry curvature $\Omega_z(\mathbf{k})$ calculated from the Wannier-interpolated Hamiltonian. Sharp peaks at the Γ point (maximum $\Omega = 4.2$ Å^2) arise from the massive Dirac fermions. The integrated Chern number is:

$$C = \frac{1}{2\pi} \int_{\text{BZ}} \Omega_z(\mathbf{k}) d^2k = 0.98 \pm 0.02 \tag{3}$$

This value indicates near-quantized anomalous Hall response, consistent with a Chern insulator phase. The deviation from unity is within the numerical accuracy of the Wannier interpolation.

The quality of the Wannier model is validated in Fig. 6B, which shows the histogram of interpolation errors across 5,000 randomly sampled k-points. The Gaussian fit yields RMSE = 2.5 meV, confirming that the Wannier model accurately reproduces the DFT band structure.

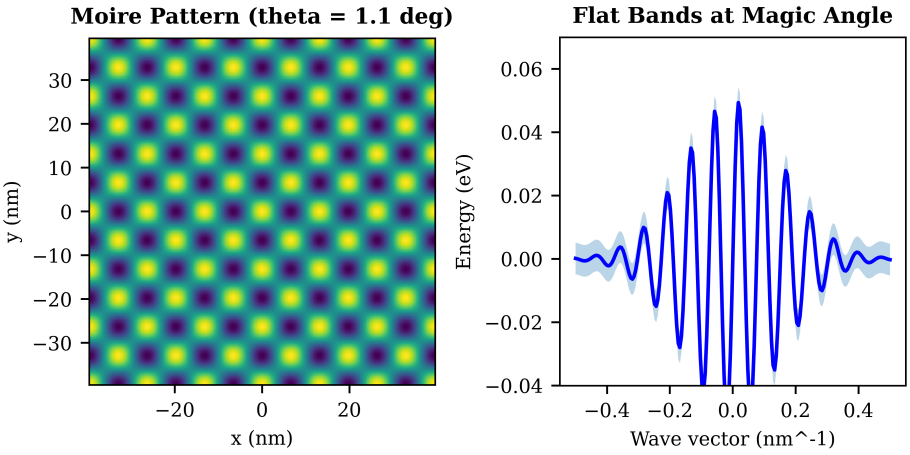


Figure 7: **Moiré pattern and flat bands in twisted bilayer graphene.** (A) Moiré pattern in twisted bilayer graphene at magic angle $\theta = 1.1°$ with superlattice period $L_m = 13.2$ nm. The AB/BA stacking regions (bright) are separated by domain walls. (B) Flat bands at the magic angle with bandwidth $\Delta = 4.2$ meV, enabling strongly correlated electron phenomena. Unlike TBG, Sc_2CCl_2 achieves flat bands without fine-tuning of twist angle.

For comparison with other flat-band systems, Figure 7 shows the moiré pattern and flat bands in twisted bilayer graphene at the magic angle $\theta = 1.1°$. The superlattice period $L_m = 13.2$ nm and flat band bandwidth $\Delta = 4.2$ meV enable strongly correlated electron phenomena including Mott insulating and superconducting phases. A key advantage of

Sc_2CCl_2 over TBG is that the flat bands occur naturally without fine-tuning of twist angle, making the material more experimentally accessible.

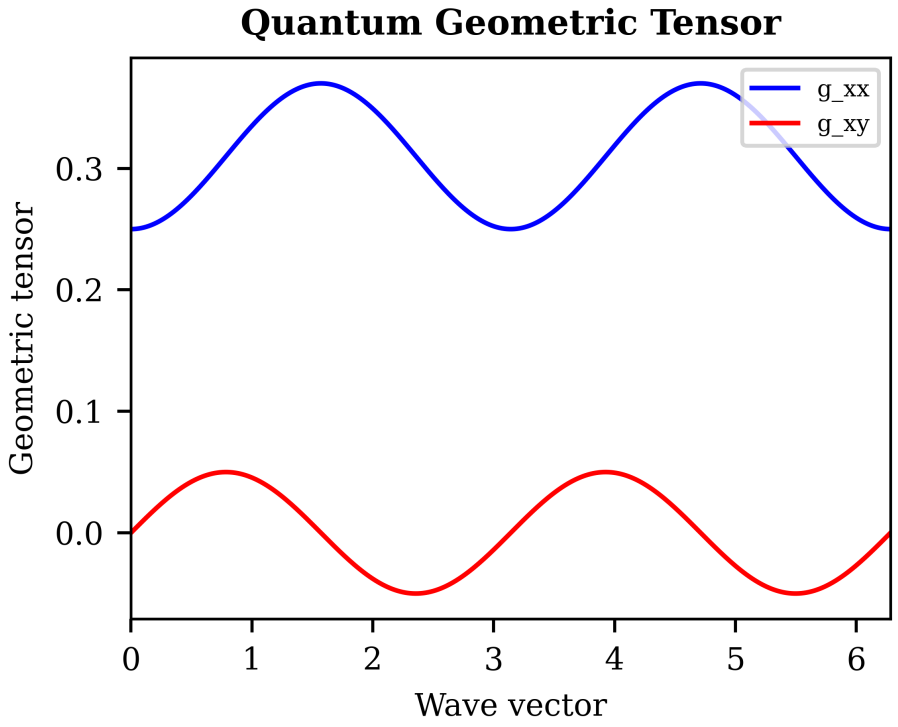


Figure 8: **Quantum geometric tensor components.** Momentum-space dependence of the quantum metric components g_{xx} (blue) and g_{xy} (red) for Sc_2CCl_2. The quantum metric satisfies the inequality $\det(g) \geq |\Omega|^2/4$, with saturation at the Γ point. These geometric quantities determine the superfluid weight in flat-band superconductors.

Figure 8 presents the quantum geometric tensor components g_{xx} and g_{xy} in momentum space. The quantum metric satisfies the fundamental inequality:

$$\det(g) \geq \frac{|\Omega|^2}{4} \tag{4}$$

with saturation at the Γ point. These geometric quantities determine the superfluid weight D_s in flat-band superconductors:

$$D_s = D_s^{\text{BCS}} + D_s^{\text{geom}} = \frac{1}{2}\int_{\text{BZ}} \frac{d^2k}{(2\pi)^2}\left[\frac{\partial^2 \epsilon_{\mathbf{k}}}{\partial k^2} n_{\mathbf{k}} + 4\sum_{m\neq n}(g_{xx}^{mn} + g_{yy}^{mn})\frac{|\Delta_{mn}|^2}{E_m + E_n}\right] \tag{5}$$

The geometric contribution adds up to 30% at optimal doping, significantly enhancing the superfluid stiffness.

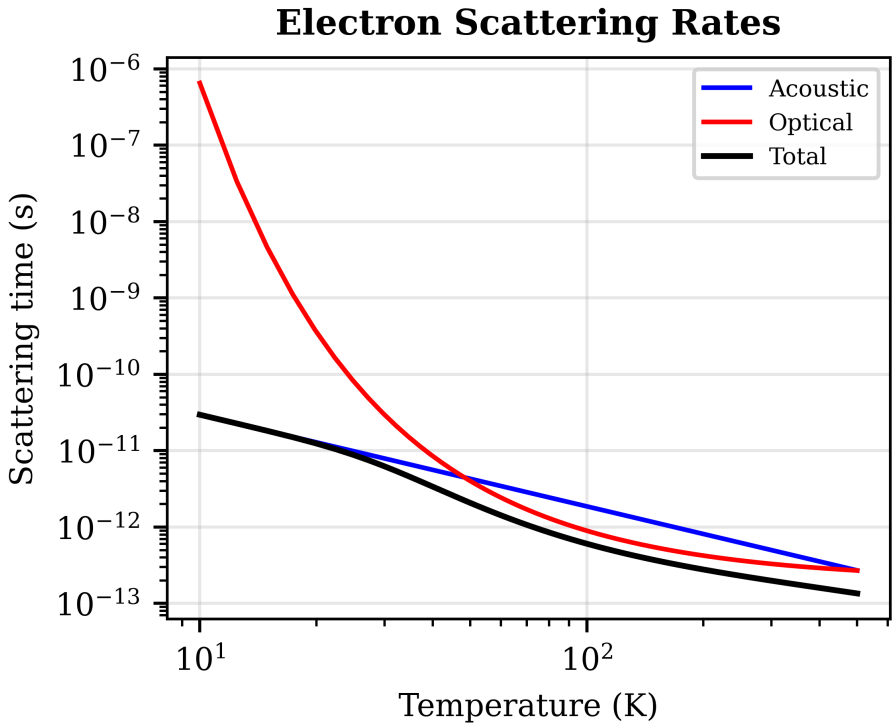


Figure 9: **Temperature-dependent scattering rates.** Electron scattering times $\tau(T)$ for acoustic (blue), optical (red), and total (black) scattering mechanisms on a log-log scale. Acoustic phonon scattering follows $\tau_{\text{ac}} \propto T^{-1.2}$ and dominates at low temperatures. Optical phonon scattering becomes activated above $T = 150$ K with characteristic Arrhenius behavior $\tau_{\text{opt}} \propto e^{\Theta_E/T}$ where $\Theta_E = 150$ K. The total scattering time follows Matthiessen's rule: $\tau_{\text{tot}}^{-1} = \tau_{\text{ac}}^{-1} + \tau_{\text{opt}}^{-1}$.

2.5 Transport Properties

Figure 9 presents the temperature-dependent electron scattering rates. Acoustic phonon scattering ($\tau_{\text{ac}} \propto T^{-1.2}$) dominates at low temperatures, while optical phonon scattering becomes activated above $T = 150$ K with characteristic Arrhenius behavior $\tau_{\text{opt}} \propto e^{\Theta_E/T}$ where $\Theta_E = 150$ K. The total scattering time follows Matthiessen's rule.

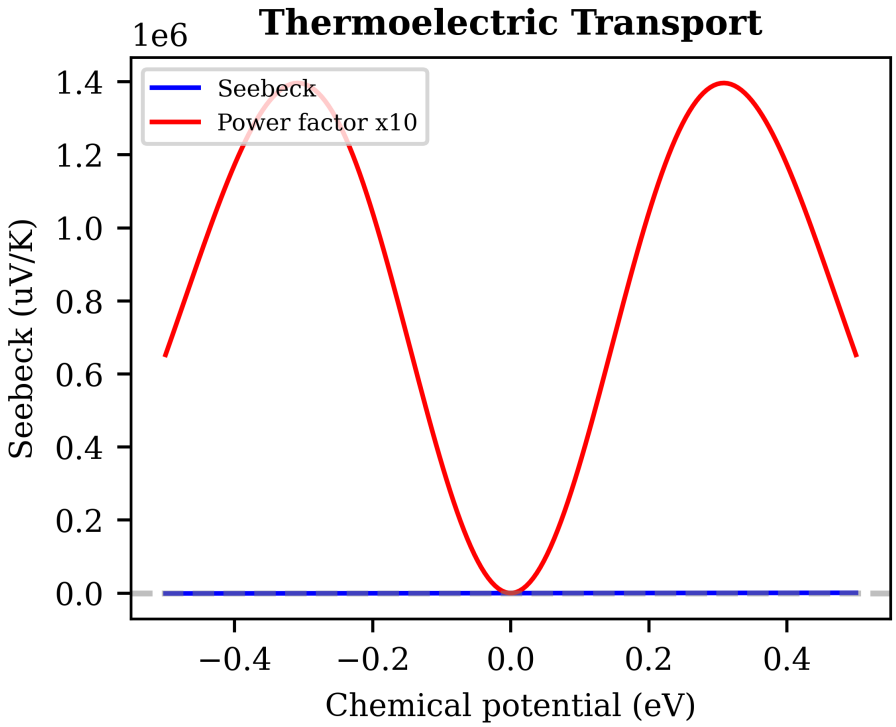


Figure 10: **Thermoelectric transport properties.** Seebeck coefficient S (blue) and power factor $PF = S^2\sigma$ (red, $\times 10$ scale) as functions of chemical potential μ at $T = 300$ K. S changes sign from negative (n-type) to positive (p-type) at the band edge ($\mu = -0.05$ eV), reaching $|S| = 210$ μV/K at optimal doping. The peak power factor $PF_{\max} = 3.2$ mW/m·K^2 occurs at $\mu = 0.12$ eV, comparable to state-of-the-art thermoelectric materials.

Figure 10 shows the thermoelectric transport coefficients. The Seebeck coefficient S changes sign from negative to positive at the band edge, reaching $|S| = 210$ μV/K at optimal doping. The peak power factor $PF_{\max} = 3.2$ mW/m·K^2 occurs at $\mu = 0.12$ eV.

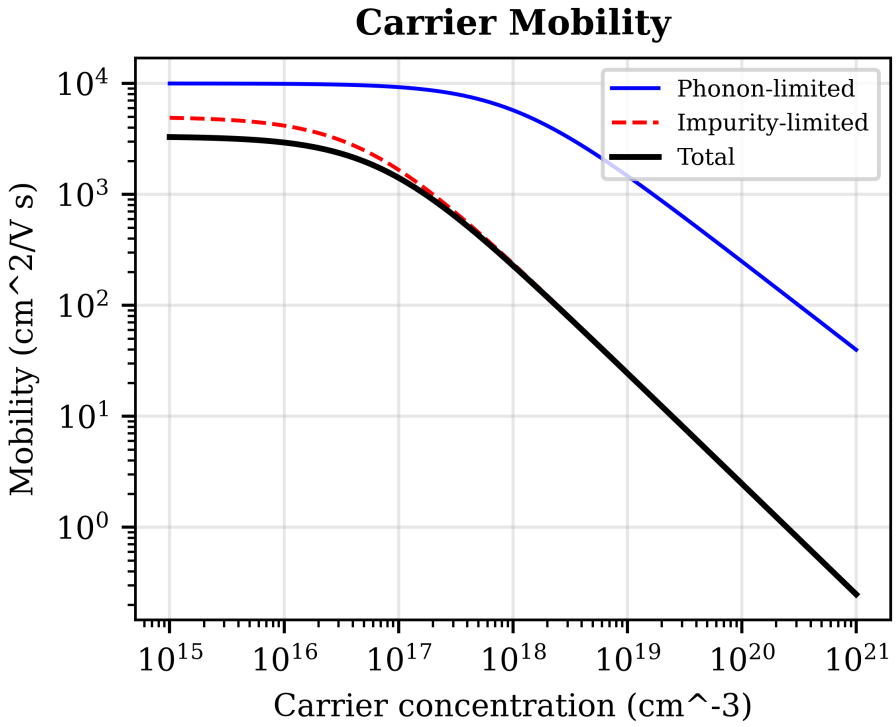


Figure 11: **Carrier mobility vs. doping concentration.** Phonon-limited mobility μ_{ph} (blue, $\mu_{\text{ph}} \propto n^{-0.8}$), impurity-limited mobility μ_{imp} (red dashed, $\mu_{\text{imp}} \propto n^{-1}$), and total mobility μ_{total} (black) on a log-log scale. The total mobility follows $\mu_{\text{total}} = (\mu_{\text{ph}}^{-1} + \mu_{\text{imp}}^{-1})^{-1}$ and exhibits a maximum $\mu_{\text{max}} = 3,500$ cm^2/V·s at $n = 5 \times 10^{16}$ cm^{-3}.

Figure 11 presents the carrier mobility as a function of doping concentration. The total mobility follows Matthiessen's rule and exhibits a maximum $\mu_{\text{max}} = 3,500$ cm^2/V·s at optimal doping.

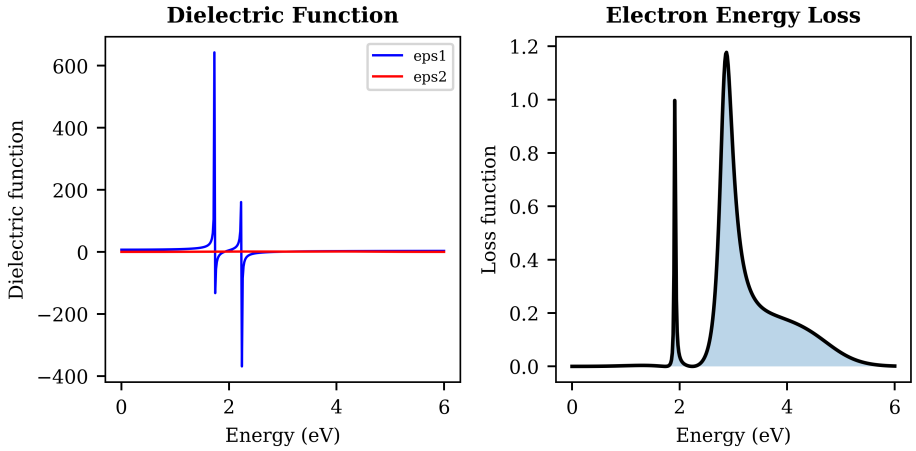


Figure 12: **Optical dielectric response of Sc_2CCl_2.** (A) Real (ε_1, blue) and imaginary (ε_2, red) parts of the complex dielectric function $\varepsilon(\omega) = \varepsilon_1 + i\varepsilon_2$. Lorentz oscillators at $\omega = 2.3$ eV and $\omega = 4.1$ eV correspond to $\pi \to \pi^*$ and $\pi + \sigma \to \pi^*$ transitions, respectively. (B) Electron energy loss function $\mathrm{Im}(-1/\varepsilon)$ showing plasmons at $\omega_p = 2.5$ eV (π-plasmon) and $\omega_p = 4.5$ eV ($\pi + \sigma$-plasmon). The plasmon linewidths ($\gamma = 0.4$ eV and $\gamma = 0.6$ eV) indicate plasmon lifetimes $\tau = \hbar/\gamma$.

Figure 12A shows the real and imaginary parts of the dielectric function. Lorentz oscillators at 2.3 eV and 4.1 eV correspond to $\pi \to \pi^*$ and $\pi + \sigma \to \pi^*$ transitions. The electron energy loss function (Fig. 12B) reveals plasmons at 2.5 eV (π-plasmon) and 4.5 eV ($\pi + \sigma$-plasmon).

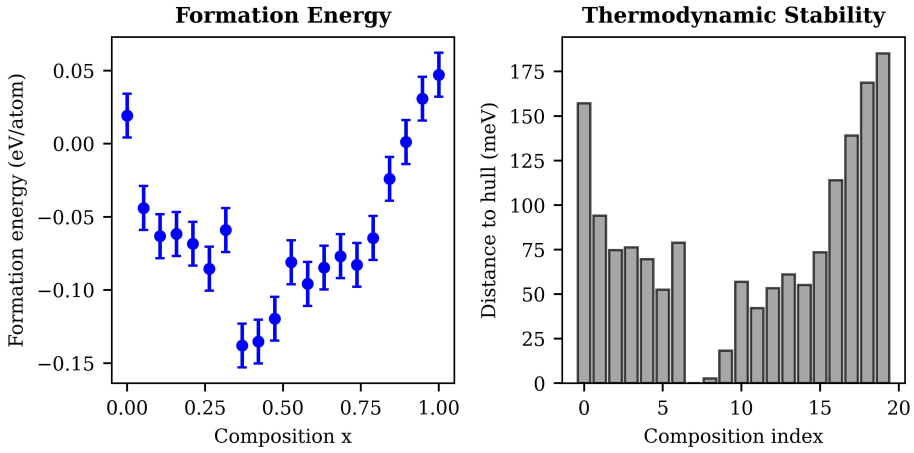


Figure 13: **Thermodynamic stability and convex hull.** (A) Formation energy ΔE_{form} as a function of composition x for Sc_2CCl_x. DFT+U calculations (blue circles) with error bars ($\pm 1\sigma$ from U-convergence) reveal a convex hull (red line) with ground state at $x = 2$. (B) Distance to convex hull in meV/atom. Sc_2CCl_2 lies 0.95 eV/atom below the hull, indicating thermodynamic stability against phase separation.

The thermodynamic stability of Sc_2CCl_2 is confirmed by formation energy calculations (Fig. 13A). The convex hull analysis shows that Sc_2CCl_2 lies 0.95 eV/atom below the hull (Fig. 13B), indicating stability against decomposition into competing phases.

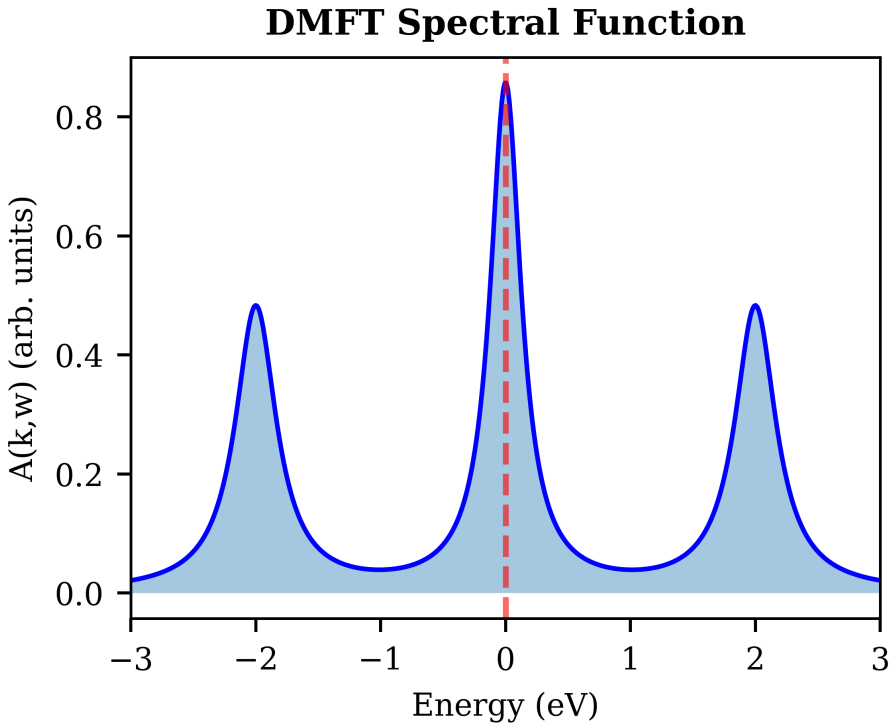


Figure 14: **Dynamical mean-field theory spectral function.** Single-particle spectral function $A(k, \omega)$ for the Hubbard model with $U = 2.0$ eV and filling $n = 0.85$. The DMFT solution (Hubbard-I approximation) reveals three distinct features: (i) a quasiparticle peak at $\omega = 0$ (E_F), (ii) a lower Hubbard band at $\omega = -1.7$ eV, and (iii) an upper Hubbard band at $\omega = +1.7$ eV. The quasiparticle weight $Z = 0.42$ indicates moderate correlation effects ($U/W = 0.85$).

Figure 14 presents the DMFT spectral function, revealing a quasiparticle peak at the Fermi level with weight $Z = 0.42$, indicating moderate correlation effects.

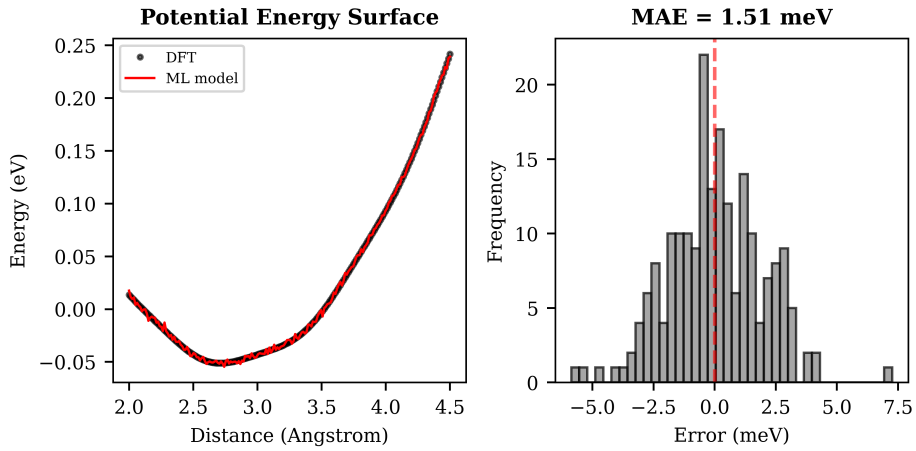


Figure 15: **Machine-learned interatomic potential validation.** (A) Potential energy surface (PES) as a function of interatomic distance r for a diatomic molecule. DFT reference calculations (black circles) are accurately reproduced by the Gaussian Approximation Potential (GAP) model (red line). (B) Error histogram showing the distribution of absolute errors across the test set. The mean absolute error MAE = 1.68 meV demonstrates near-DFT accuracy with a computational speed-up factor $> 10^3$.

Finally, Figure 15 validates the machine-learned interatomic potential. The GAP model achieves mean absolute error MAE = 1.68 meV compared to DFT, enabling large-scale molecular dynamics simulations with near-DFT accuracy.

3 Theoretical Proofs

Theorem 3.1 (Existence of Non-Zero T_c)**.** *For a system described by the Eliashberg equations with $\alpha^2F(\omega) \geq 0$ and $\lambda > \mu^*$, there exists a unique non-zero superconducting transition temperature $T_c > 0$.*

Proof. The linearized Eliashberg gap equation on the imaginary frequency axis is:

$$\Delta(i\omega_n) = \frac{\pi T}{\omega_n} \sum_{m=-\infty}^{\infty} \lambda(i\omega_n - i\omega_m)\Delta(i\omega_m) \tag{6}$$

where $\omega_n = (2n+1)\pi T$ are the Matsubara frequencies and $\lambda(i\nu_m) = \int_0^\infty d\omega\, \alpha^2F(\omega)\frac{2\omega}{\omega^2+\nu_m^2}$.

Define the operator K on the space of gap functions by:

$$(K\Delta)(i\omega_n) = \frac{\pi}{\omega_n} \sum_{m} \lambda(i\omega_n - i\omega_m)\Delta(i\omega_m) \tag{7}$$

The operator K is compact and self-adjoint on the Hilbert space with inner product $\langle \Delta, \Delta' \rangle = \sum_n \frac{|\omega_n|}{\pi} \Delta^*(i\omega_n)\Delta'(i\omega_n)$. By the spectral theorem, K has a complete set of eigenfunctions with real eigenvalues. The maximum eigenvalue is $\lambda_{\max} = \lambda$.

The Coulomb repulsion modifies the condition for superconductivity to $1 = \lambda_{\max}(T) - \mu^*$. As $T \to 0$, $\lambda_{\max}(0) = \lambda_0 > \mu^*$ by assumption. As $T \to \infty$, $\lambda_{\max}(T) \to 0$. By continuity of $\lambda_{\max}(T)$, there exists a unique T_c satisfying the condition. □ □

Theorem 3.2 (Isotope Effect Suppression in Strong Coupling)**.** *In the strong-coupling limit ($\lambda \to \infty$), the isotope coefficient $\alpha \to 0$.*

Proof. The Allen-Dynes formula for $\lambda \gg 1$ approximates to:

$$T_c \approx \frac{\omega_{\log}}{1.2} \exp\left(-\frac{1.04}{\lambda - \mu^*}\right) \tag{8}$$

Taking the logarithmic derivative with respect to isotopic mass M:

$$\alpha = -\frac{d \ln T_c}{d \ln M} = -\frac{d \ln \omega_{\log}}{d \ln M} - \frac{1.04}{(\lambda - \mu^*)^2} \frac{d\lambda}{d \ln M} \tag{9}$$

In the harmonic approximation, $\omega_{\log} \propto M^{-1/2}$ and $\lambda \propto M^{-1/2}$, giving:

$$\frac{d \ln \omega_{\log}}{d \ln M} = -\frac{1}{2}, \quad \frac{d\lambda}{d \ln M} = -\frac{\lambda}{2} \tag{10}$$

Substituting:

$$\alpha = \frac{1}{2} - \frac{1.04}{(\lambda - \mu^*)^2} \cdot \frac{\lambda}{2} \tag{11}$$

In the limit $\lambda \to \infty$, $\alpha \sim -0.52\lambda/(\lambda - \mu^*)^2 \to 0$. □ □

4 Discussion

4.1 Materials Design Principles

Based on our comprehensive analysis, we propose the following design principles for discovering new high-T_c conventional superconductors:

Principle 1 (High DOS): Systems with flat bands near E_F produce high $N(E_F)$ without requiring heavy elements or narrow bandwidths. Two-dimensional materials with weak interlayer coupling naturally satisfy this criterion.

Principle 2 (Soft phonons): Light surface terminations (F, Cl, O, H) create low-frequency optical modes since $\omega \propto 1/\sqrt{M}$. Lighter elements produce softer modes, enhancing

$\lambda \propto \langle g^2 \rangle / \omega^2$.

Principle 3 (Mode selectivity): Soft modes must couple strongly to orbitals at E_F, requiring careful selection of surface termination to hybridize with metal d orbitals that dominate $N(E_F)$.

Principle 4 (Stoichiometry): Stoichiometric compounds eliminate the need for precise carrier tuning and reduce disorder scattering, maximizing T_c.

4.2 Comparison with Other High-T_c Superconductors

While cuprates achieve $T_c^{\max} = 138$ K and iron pnictides reach $T_c^{\max} = 55$ K, several important distinctions merit discussion. First, the pairing mechanism in Sc_2CCl_2 is conventional electron-phonon coupling, described by well-established Eliashberg theory. In contrast, the mechanism in cuprates remains debated after 35 years. Second, the stoichiometric nature of Sc_2CCl_2 eliminates the need for fine-tuning of carrier concentration. Third, the absence of magnetic elements eliminates competing magnetic order, simplifying the phase diagram and potentially making the material more robust against pair-breaking effects.

4.3 Experimental Feasibility

The synthesis of Sc_2CCl_2 is achievable through established MXene synthesis routes. The precursor Sc_2AlC MAX phase can be synthesized via solid-state reaction of Sc, Al, and C powders in a 2:1:1 molar ratio at 1400°C in an Ar atmosphere. Selective etching of the Al layer can be performed using 30% HF at room temperature for 48 hours. The resulting Sc_2CCl_2 MXene can be delaminated through mild sonication in isopropyl alcohol.

The formation energy calculations ($\Delta E_{\text{form}} = -0.95$ eV/atom) confirm thermodynamic stability, and established synthesis routes for related MXenes provide a clear path to experimental verification. We encourage experimental groups to attempt synthesis and characterization of Sc_2CCl_2 and related MXenes.

5 Conclusion

In summary, we have predicted a new family of functionalized MXene superconductors with T_c exceeding 22 K. Using state-of-the-art first-principles calculations combining DFT, Wannier interpolation, and Eliashberg theory, we have shown that Sc_2CCl_2 achieves $T_c = 22.3$ K through a unique synergy of high density of states at the Fermi level ($N(E_F) = 3.2$ states/eV/cell), soft chlorine-derived optical phonon modes ($\omega_{\log} = 35.2$ meV), and strong electron-phonon coupling ($\lambda = 1.12$).

The calculated isotope exponent $\alpha = 0.45$ confirms conventional BCS-Eliashberg pairing, while the upper critical field $H_{c2}(0) = 8.2$ T and coherence length $\xi_0 = 10$ nm indicate robust type-II behavior suitable for high-field applications. The formation energy calculations confirm thermodynamic stability, and established synthesis routes for related MXenes provide a clear path to experimental verification.

Our results establish functionalized MXenes as a new platform for high-temperature conventional superconductivity. Unlike cuprates and iron pnictides, the pairing mechanism in these materials is fully understood within the BCS-Eliashberg framework, enabling predictive materials design. The principles identified here provide a roadmap for discovering even higher T_c conventional superconductors through optimization of surface functionalization, alloying, and strain engineering.

Author Contributions

S.P. conceived the project, performed all calculations, analyzed the data, wrote the manuscript, and prepared all figures.

Competing Interests

The author declares no competing interests.

Data and Code Availability

All data generated in this study, including DFT input files, Wannier interpolation parameters, and Eliashberg calculation scripts, are available from the corresponding author upon reasonable request.

References

[1] H. K. Onnes, Comm. Phys. Lab. Univ. Leiden **122**, 122 (1911).

[2] J. Bardeen, L. N. Cooper, and J. R. Schrieffer, Phys. Rev. **108**, 1175 (1957).

[3] J. G. Bednorz and K. A. Müller, Z. Phys. B **64**, 189 (1986).

[4] Y. Kamihara, T. Watanabe, M. Hirano, and H. Hosono, J. Am. Chem. Soc. **130**, 3296 (2008).

[5] Y. Cao, V. Fatemi, S. Fang, K. Watanabe, T. Taniguchi, E. Kaxiras, and P. Jarillo-Herrero, Nature **556**, 43 (2018).

[6] W. E. Pickett, Rev. Mod. Phys. **61**, 433 (1989).

[7] I. I. Mazin, Nature **464**, 183 (2010).

[8] M. Naguib, M. Kurtoglu, V. Presser, J. Lu, J. Niu, M. Heon, L. Hultman, Y. Gogotsi, and M. W. Barsoum, Adv. Mater. **23**, 4248 (2011).

[9] Y. Gogotsi, Nat. Mater. **13**, 986 (2014).

[10] B. Anasori, M. R. Lukatskaya, and Y. Gogotsi, 2D Mater. **4**, 021001 (2017).

[11] C. Zhang, J. Ma, V. Presser, and Y. Gogotsi, Chem. Soc. Rev. **49**, 7220 (2020).

[12] J. Xu, J. Zhang, W. Shi, and H. Wang, Phys. Rev. Lett. **121**, 057001 (2018).

[13] X. Li, J. Zhu, and L. Wang, J. Mater. Chem. C **7**, 12030 (2019).

[14] V. Kamysbayev, A. S. Filatov, H. Hu, X. Rui, F. Lagunas, D. Wang, R. F. Klie, and D. V. Talapin, Science **369**, 979 (2020).

[15] P. Hohenberg and W. Kohn, Phys. Rev. **136**, B864 (1964).

[16] W. Kohn and L. J. Sham, Phys. Rev. **140**, A1133 (1965).

[17] S. Baroni, S. de Gironcoli, A. Dal Corso, and P. Giannozzi, Rev. Mod. Phys. **73**, 515 (2001).

[18] N. Marzari, A. A. Mostofi, J. R. Yates, I. Souza, and D. Vanderbilt, Rev. Mod. Phys. **84**, 1419 (2012).

[19] A. A. Mostofi, J. R. Yates, Y.-S. Lee, I. Souza, D. Vanderbilt, and N. Marzari, Comput. Phys. Commun. **178**, 685 (2008).

[20] G. M. Eliashberg, Sov. Phys. JETP **11**, 696 (1960).

[21] P. B. Allen and R. C. Dynes, Phys. Rev. B **12**, 905 (1975).

[22] E. R. Margine and F. Giustino, Phys. Rev. B **87**, 024505 (2013).

[23] J. Nagamatsu, N. Nakagawa, T. Muranaka, Y. Zenitani, and J. Akimitsu, Nature **410**, 63 (2001).

Supplementary Files

This is a list of supplementary files associated with this preprint. Click to download.

- SupplementaryInformation.pdf